Tectonophysics 774 (2020) 228297

Contents lists available at ScienceDirect

Tectonophysics

journal homepage: www.elsevier.com/locate/tecto

# Seismic evidence links the subducted Mongol-Okhotsk slab to deformation in D″ near the northeastern margin of the Perm Anomaly

Juntao Tao[a], Jinfeng Hu[a], Cong Jin[b], Xiaobo He[c,*]

[a] Department of Marine Sciences, Zhejiang University, Zhoushan 316021, China
[b] Zhejiang Institute of Geology and Mineral Resource, Hangzhou 310007, China
[c] Department of Geophysics, Yunnan University, Kunming, 650091, China

ARTICLE INFO

*Keywords:*
The D″ discontinuity
The Perm Anomaly
Seismic anisotropy
LLSVPs
The Mongol-Okhotsk slab

ABSTRACT

Numerical simulations have indicated that the Large low-Shear Velocity Provinces (LLSVPs) dynamically interact with subducted slabs in D″, and slabs in turn play an important role in influencing the shape and location of the LLSVPs. In this study, we find evidence for the existence of the D" discontinuity near the northeastern margin of the Perm Anomaly — a smaller LLSVP beneath Eurasia, by analyzing the *Scd* (the lower mantle triplication) phases generated from two deep events occurring in the northwestern Pacific subduction zone and recorded at stations in Europe and Turkey. The D″ discontinuity in the north is characterized with a +2% velocity increase occurring at a height of 300 km above the core-mantle boundary (CMB), whereas the discontinuity in the south is characterized with a +3% velocity increase occurring at a height of 260 km above the CMB. The D″ discontinuity is most likely attributed to a phase transition from perovskite to post-perovskite in conjunction with the presence of relic slab materials (likely related to the subducted Mongol-Okhotsk slab). Our observations– along with previous seismic anisotropic detections– provide a clue to dynamically link the subducted slab to deformation taking place near the edges of the LLSVP.

## 1. Introduction

The lower mantle is composed of two large structures with anomalously low shear velocities, known as Large Low-Shear Velocity Provinces (LLSVPs), one under Africa and the other under the mid-Pacific (e.g., Simmons et al., 2010; Ritsema et al., 2011; Lekic et al., 2012; French and Romanowicz, 2015). Anomalies in both temperature and composition are likely required to explain the LLSVPs (e.g., McNamara and Zhong, 2005). Numerical simulations have predicted that the LLSVPs dynamically interact with subducted slab materials and the ambient mantle flow field at the base of the mantle (e.g., Tan et al., 2011). Passive thermochemical piles shaped by mantle convection (e.g., McNamara and Zhong, 2005) or long-lived structures over much of Earth history (Dziewonski et al., 2010) have been proposed to explain the origin and evolution of LLSVPs.

The LLSVPs are often characterized by high-density (Ishii and Tromp, 1999; Lau et al., 2017) and sharp lateral velocity gradients at their edges that extend up to ~1000 km above the core-mantle boundary (CMB) (e.g., Frost and Rost, 2014; Ni et al., 2002). Ultra-low velocity zones are also found to preferentially reside in the vicinity near the edges of the LLSVPs (e.g., Ma et al., 2019; Rost et al., 2010). Moreover, at least some of the surface hotspots and Large Igneous Provinces (LIPs) are likely to be derived from deep mantle plumes that originated from the D″ region near the edges of the LLSVPs (e.g., Burke et al., 2008; Steinberger and Torsvik, 2012; Thorne et al., 2004; Torsvik et al., 2006). Therefore, probing the structure near the edges of LLSVPs will contribute to improving our understanding of relevant dynamics.

Recent studies have observed strong seismic anisotropy occurring in the lowermost mantle near the edges of the African and Pacific LLSVPs, suggesting deformation concentrated at LLSVP boundaries (e.g., Cottaar and Romanowicz, 2013; Deng et al., 2017; Ford et al., 2015; Grund and Ritter, 2019; Lynner and Long, 2014; Wang and Wen, 2007). The presence of subducted slab materials residing adjacent to the Pacific LLSVP also have been detected (e.g., Idehara et al., 2013; Ma et al., 2016; Sun et al., 2019). However, existence of both seismic anisotropy and slab-like fast anomalies near the boundaries of LLSVPs has not often been seen, leading to a lack of evidence for dynamic linking subducted slabs in addition to LLSVPs with deformation taking place in the deep mantle.

In this study, we aim to probe the D″ discontinuity in the lowermost mantle near the boundaries of the Perm Anomaly, which has a similar reduction in seismic velocity but smaller size compared to the African and Pacific LLSVPs (Lekic et al., 2012). The Perm Anomaly has been

* Corresponding author.
*E-mail addresses:* xb_he@126.com, xbhe@zju.edu.cn (X. He).

https://doi.org/10.1016/j.tecto.2019.228297
Received 2 June 2019; Received in revised form 17 November 2019; Accepted 21 November 2019
Available online 23 November 2019

suggested to separate from the African LLSVP by the Balkan slab (van der Meer et al., 2018) and it has been either linked with the Emeishan large igneous provinces (Flament et al., 2017) or the Siberian Traps (Torsvik and Domeier, 2017). We employ detections of *Scd* arrivals (the lower mantle *S* wave triplication) (e.g., Hu and He, 2019; Shen et al., 2014; Sun et al., 2016; Whittaker et al., 2016; Yao et al., 2015) to locate the D″ discontinuity at the base of the mantle adjacent to the Perm Anomaly.

The top of the D″ layer is referred as the D″ discontinuity, which often has a sharp increase in *S*-wave speed of 2–3 % and smaller increase in *P*-wave velocity, and is situated about 100–450 km above the core-mantle boundary (e.g., Cobden and Thomas, 2013). Different behaviors of the D″ discontinuity also possibly exist. The D″ discontinuity has been widely considered as a result of a phase transition from perovskite to post-perovskite (e.g., Murakami et al., 2004; Oganov and Ono, 2004; Shim et al., 2004) after it was first observed by Lay and Helmberger (1983) about three decades ago. Nonetheless, the D″ discontinuity is occasionally difficult to reconcile with a simple phase transition; lateral variations in lower mantle composition are thought to complicate the origin of the discontinuity (e.g., Cobden and Thomas, 2013). In addition, the presence of a relic slab also plays an important role in the detectability of the D″ discontinuity because the pv-ppv transition in harzburgite and MORB is seismologically detectable due to Al effects (e.g., Dorfman and Duffy, 2014; Grocholski et al., 2012; Sun et al., 2018). Therefore, detections of D″ discontinuity can in turn serve as evidence of the presence of paleoslab materials in D″.

A recent study has shown the existence of a paleoslab (likely associated with the Paleotethyan slab) in the lowermost mantle residing adjacent to the southeastern edge of the Perm Anomaly (Hu and He, 2019). Fritzell et al. (2016)'s geodynamic modeling results suggested that the subducted Mongol-Okhotsk slab in the lowermost mantle may have played an important role in influencing the formation and evolution of the Perm Anomaly at the northeastern margin. In this study, we find evidences for the existence of the D″ discontinuity near the northeastern Perm Anomaly border, which may be related to the subducted Mongol-Okhotsk slab at the CMB. Along with previous seismic anisotropic observations in the neighboring areas in D″ (e.g., Grund and Ritter, 2019; Long and Lynner, 2015; Wookey and Kendall, 2008), our detections may thus shed light on the interactions of the LLSVPs with the subducting slabs in the lowermost mantle occurring near the boundaries of the LLSVPs.

## 2. Data and methods

Our purpose here is to locate slab remnants in D″ surrounding the Perm Anomaly, in particular near its northeastern edge. Seismic pairs like *S-ScS* (e.g., He and Wen, 2011) and *SKS-SKKS* (e.g., Zhang et al., 2009) that have similar path in the upper mantle, but significantly different ones in the lowermost mantle and D″, are often used not only to characterize the seismic anisotropy (e.g., Restivo and Helffrich, 2006), but also to constrain the seismic heterogeneity (e.g., Ma et al., 2016; Rao and Kumar, 2014) in the lowermost mantle by analyzing their differential traveltimes. Precursors to the core phase *PKP* or *PKKP* are also useful to locate scatterers in D″ (e.g., Frost et al., 2017; Waszek et al., 2015). In this paper, we analyzed *Scd* arrivals – a lowermost mantle triplicated wave that occurs as the down-going *S* wave and refracts below the D″ discontinuity (e.g., Hu and He, 2019; Sun et al., 2016; Yao et al., 2015) – to investigate the D″ discontinuity sampling the northeastern edge of the Perm Anomaly (Fig. 1). The existence of the D″ discontinuity is often associated with the presence of slab remnants at the base of the mantle (e.g., Dorfman and Duffy, 2014; Grocholski et al., 2012).

The *Scd* arrivals are recorded by two arrays in Europe and Turkey from two earthquakes in the northwestern Pacific subduction zone (Fig. 1), respectively. Specifically, the event occurred in the Kuril subduction zone on October 21, 2011 was recorded by a network comprising 34 stations in Turkey; whereas the event occurred in the Japan subduction zone on April 5, 2013 was recorded by a network comprising 79 stations in northwestern Europe. All the stations used in this study are permanent. The events (from USGS event catalog) with moderate magnitude ($5.8 < Mw < 7$) were selected to limit the duration of source time function (e.g., Sun et al., 2016).

We also plotted a map in Fig. S1 of the Supporting information showing the distribution of *ScS* bounce points in which those from four events are corresponding to the record-sections with blurred *Scd* arrivals (Fig. S2), and those from 54 events are corresponding to the record-sections with no clear *Scd* arrivals. The information of the two events and their receivers used in this study are listed in Tables 1 and S1–S2 of the supporting information, respectively. The information of the 54 events with no clear *Scd* arrivals and 4 events with blurred *Scd* arrivals along with their receivers are listed in Tables S3–S5 of the supporting information, respectively.

The instrument responses have been deconvolved from the observed seismograms, and the original horizontal components were rotated to the tangential (*SH*) and radial (*SV*) components. We applied a two-pass, two-pole Butterworth band-pass filter with corner frequencies at 0.05 and 0.5 Hz to the data, and visually selected arrivals with high signal-to-noise ratio for *Scd* waveform analyses. All the records in tangential component are aligned along the *S* arrivals (Fig. 2a and d) and are stacked over 0.5° distance intervals (Fig. 2b and e) to suppress the incoherent noise. The number of stacking traces for each bin is also shown atop each trace at right. A clear *Scd* arrival is noticeable in between *S* and *ScS* on the data sections (Fig. 2a and d). The two record-sections in radial component for the two events used in this study are presented in Fig. S3. Due to the interferences of $P - SV$ conversions, the *Scd* arrivals in radial components are less prominent compared to tangential components. Synthetic seismograms were calculated to compare with the data with a purpose of finding the suitable model to explain the observations according to a propagation matrix algorithm (Wang, 1999). This algorithm uses the same strategy as the original propagator algorithm (i.e., the Thomson-Haskell propagator algorithm Thomson, 1950; Haskell, 1953), which calculates the displacement vector in the frequency-wavenumber domain from layer to layer via a chain rule, but Wang 's (1999) algorithm avoids the numerical problem by inserting an additional numerical procedure into the matrix propagation loop (the detailed description about the propagator algorithm can be referred to Wang, 1999).

In order to determine the velocity profile of the D″ discontinuity, we compared data and synthetic predictions by minimizing the travel time, slowness and amplitude misfits according to the strategy suggested by Hu and He (2019), and the calculation equations are as follows:

$$\delta T = \frac{1}{n}\sum_{i=1}^{n}\sqrt{\left(\frac{\delta T^{syn}_{Scd_i-S_i} - \delta T^{obs}_{Scd_i-S_i}}{\delta T^{obs}_{Scd_i-S_i}}\right)^2 + \left(\frac{\delta T^{syn}_{ScS_i-S_i} - \delta T^{obs}_{ScS_i-S_i}}{\delta T^{obs}_{ScS_i-S_i}}\right)^2} \quad (1)$$

$$\delta U = \sqrt{\left(\frac{\delta U^{syn}_{Scd-S} - \delta U^{obs}_{Scd-S}}{\delta U^{obs}_{Scd-S}}\right)^2 + \left(\frac{\delta U^{syn}_{ScS-S} - \delta U^{obs}_{ScS-S}}{\delta U^{obs}_{ScS-S}}\right)^2} \quad (2)$$

$$\delta A = \frac{1}{n}\sum_{i=1}^{n}\sqrt{\left(\frac{\delta A^{syn}_{Scd_i}/\delta A^{syn}_{S_i} - \delta A^{obs}_{Scd_i}/\delta A^{obs}_{S_i}}{\delta A^{obs}_{Scd_i}/\delta A^{obs}_{S_i}}\right)^2 + \left(\frac{\delta A^{syn}_{ScS_i}/\delta A^{syn}_{S_i} - \delta A^{obs}_{ScS_i}/\delta A^{obs}_{S_i}}{\delta A^{obs}_{ScS_i}/\delta A^{obs}_{S_i}}\right)^2} \quad (3)$$

where $\delta T$, $\delta U$ and $\delta A$ are the travel time, slowness and amplitude misfits, respectively. We applied equal weights to the three misfits, and calculated the final misfit as

$$Misfit = \frac{\delta T + \delta U + \delta A}{3} \quad (4)$$

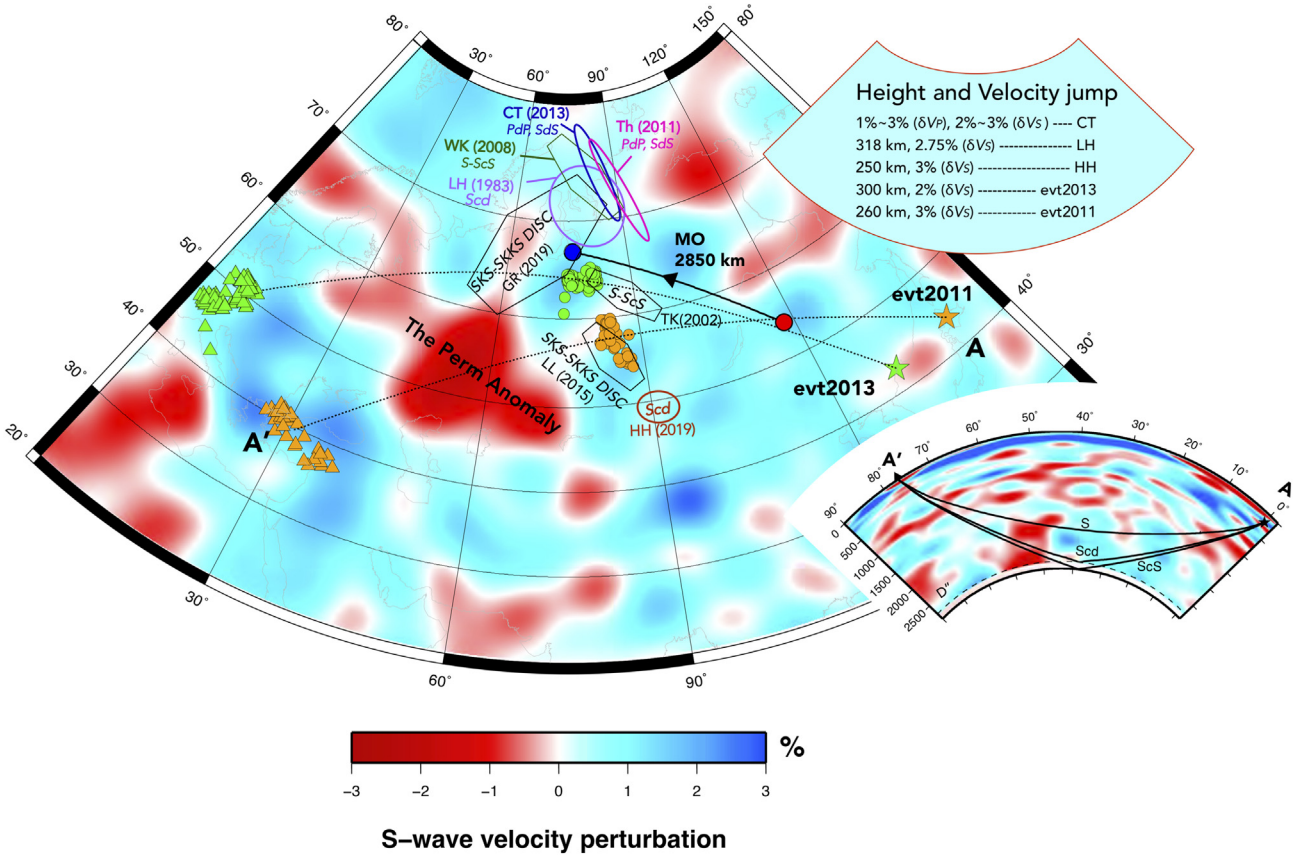


**Fig. 1.** A map demonstrating the distribution of two events (stars) with their receivers (triangles) of two isolated networks plotted atop the S40RTS tomography model (Ritsema et al., 2011). The theoretical bounce points of *ScS* on the CMB as calculated by TauP (Crotwell et al., 1999) are shown as green and orange circles. Hexagons schematically depict the locations with occurrence of splitting discrepancies in *SKS-SKKS* (Grund and Ritter, 2019; Long and Lynner, 2015) and *S-ScS* (Thomas and Kendall, 2002; Wookey and Kendall, 2008). Ellipses indicate the locations with the D″ discontinuity from previous observations (Cobden and Thomas, 2013; Hu and He, 2019; Lay and Helmberger, 1983; Thomas et al., 2011). Red circle indicates geological record of the MO slab with base depth of 2850 km, blue circle represents slab midpoint projected to surface, and arrow indicates the correlation between slab and its corresponding geological record and exhibits the displacement of the geological record over time relative to the relatively fixed locations of sinking slab. The slab information is given by van der Meer et al. (2018). The right lower insert exhibits raypaths observed in our study on top of a cross section through the GyPSuM tomography model from event to station (AA′). The right upper inset lists the characteristics of the D″ discontinuity (including height and velocity jump) in this region. CMB = core-mantle boundary; MO = Mongol-Okhotsk; CT = Cobden and Thomas; Th = Thomas et al.; WK = Wookey and Kendall; LH = Lay and Helmberger; GR = Grund and Ritter; TK = Thomas and Kendall; LL = Long and Lynner; HH = Hu and He. (For interpretation of the references to color in this figure legend, the reader is referred to the web version of this article.)

**Table 1**
Information for two events used in *Scd* detections.

| Origin time (UTC) | Lat. | Lon. | Depth (km) | Magnitude (Mw) |
|---|---|---|---|---|
| 2011-10-21 08:02:37.950 | 43.89 | 142.47 | 187 | 6.1 |
| 2013-04-05 13:00:02.130 | 42.73 | 131.00 | 563 | 6.3 |

We generated synthetic seismograms based on two types of models (e.g., Hu and He, 2019), defined by the relationship between the geotherm and post-perovskite (ppv) phase boundary for different core temperatures (e.g., Hernlund et al., 2005) – including the "single-crossing" model and "double-crossing" model – which varied in the structure within the D″ layer using the IASP91 model as the background (Kennett and Engdahl, 1991). The single-crossing model is designed to characterize the D″ structure with a positive velocity jump in shear-wave velocity $V_s$ at the top of the D″ layer and a negative velocity gradient within the D″ layer (Fig. 2c and f). This kind of model has been widely employed to explain the observed *Scd* arrivals (see a review by Wysession et al., 1998). By contrast, the double-crossing model comprises the D″ structure with a positive velocity jump in $V_s$ at the top of the D″ discontinuity, and comprises a sharp but negative velocity jump within the D″ layer (i.e., exists a second discontinuity in D″ due to ppv-pv reverse transition). This kind of model has been revealed occasionally in some areas (e.g., Hernlund et al., 2005; Kawai et al., 2007). Note that, there is no change in density in our modelings. In addition, we assumed that the velocity structure above the D″ discontinuity is the same as the IASP91 model. However, the structures above the D″ discontinuity may have some effects on lower mantle *S* triplication, including both *S* and *Scd*, which would need to be kept in mind. Because all the seismograms are stacked over 0.5° distance intervals, and this stacking process may help to avoid the effects from the incoherent signals – perhaps caused by the structures above the D″ discontinuity – to some degree. It is also worth mentioning that, in some cases, the number of traces for stacking is less than 3 (Fig. 2), which may lead to unstable stacking results due to waveform incoherency of *Scd* or *S* (i.e., more data for stacking certainly results in more stable stacking results, because the incoherent signals can be suppressed significantly). Fortunately, the number of stacking with small number ($< 3$) of traces for the event 2011-10-21 is 3 (3 out of 9), whereas the number for the event 2013-04-05 is 2 (2 out of 13). As a result, the effects from the unstable stacking on the calculated misfits will not be strong, because the misfits rely on three independent parameters including amplitude, slowness, and travel-time calculated from all the stacked traces.

To obtain the suitable model, we constructed a suit of models to find

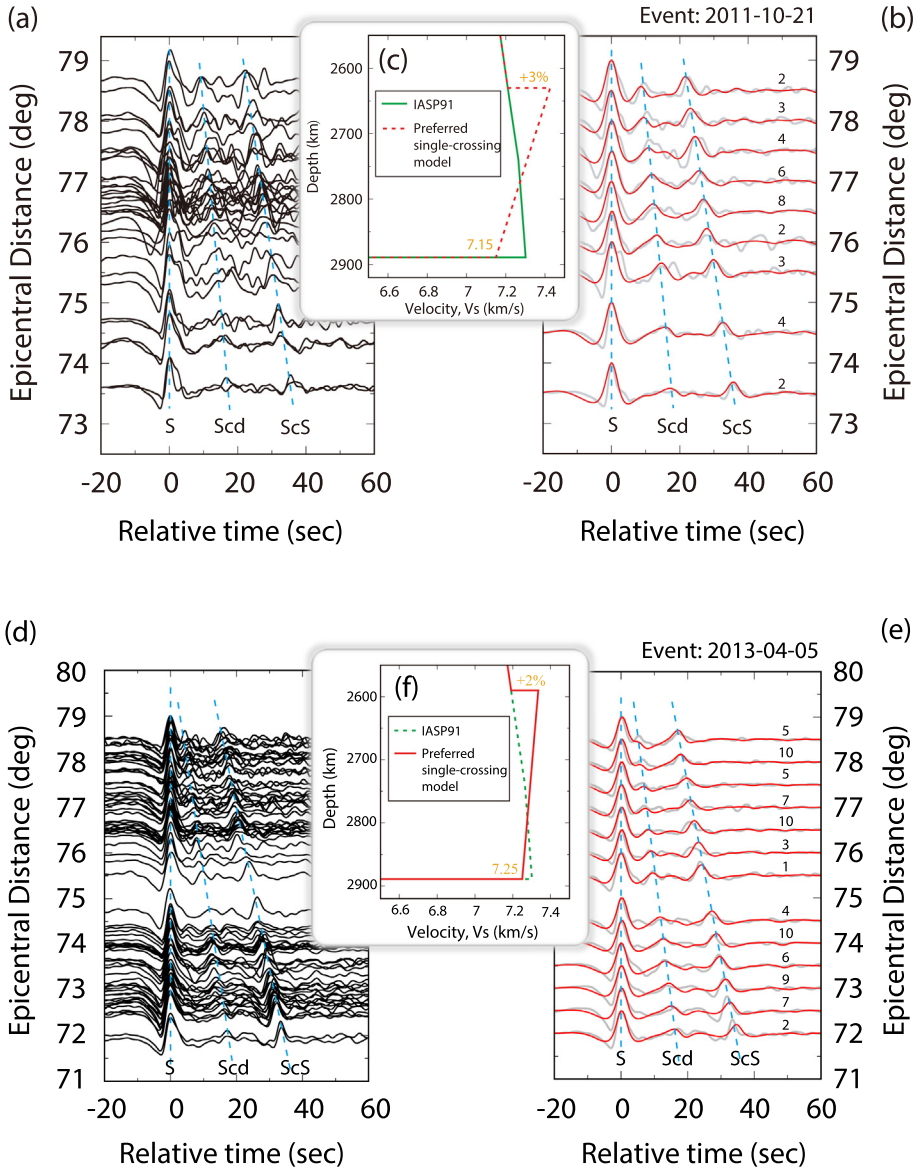


**Fig. 2.** The *SH* data without stacking for the event 2011-10-21 (a) and the event 2013-04-05 (d), respectively. Comparison of synthetics (solid red lines) calculated according to the preferred single-crossing models (c and f) and stacked (over 0.5° distance intervals *SH* data (solid grey lines)) for the event 2011-10-21 (b) and the event 2013-04-05 (e), respectively. The number of stacking traces for each bin is also shown atop each trace at right (b and e). (For interpretation of the references to color in this figure legend, the reader is referred to the web version of this article.)

the minimal misfit (Figs. 3 and 4). We varied 3 parameters including the depth of the D″ discontinuity, the velocity change in *V s* across the D″ discontinuity, and the *V s* at the CMB to generate single-crossing models; while the double-crossing models are constructed by varying the depth of the D″ discontinuity, the velocity change in *V s* across the D″ discontinuity, and the vertical spacing width of two discontinuities. We first investigated the single-crossing models, and then investigated the double-crossing models; in the end, we evaluated each preferred model of two types by calculating the fourth-root vespagrams (e.g., He and Zheng, 2018; Yang and He, 2015).

## 3. Results

### 3.1. The single-crossing model

We identify a prominent *Scd* arrival located in between the *S* and *ScS* arrivals on the record sections (Fig. 2b and e). Our results indicate that, for the event 2011-10-21 (*Scd* waves sample the D″ layer in the south (Fig. 1)), our preferred single-crossing model – to adequately replicate the data – is composed of the D″ discontinuity with a +3% velocity jump in *V s* occurring at a depth of 2630 km (i.e., the thickness of the D″ layer is 260 km) and a −2.0% velocity perturbation relative to IASP91 occurring at the CMB (Fig. 2c); whereas for the event 2013-04-05 (*Scd* waves sample the D″ layer in the north (Fig. 1)), the preferred model is characterized by the D″ discontinuity with a +2% increase in *V s* occurring at a depth of 2590 km (i.e., 300 km above the CMB) and a −0.7% velocity reduction relative to IASP91 occurring at the CMB (Fig. 2f). The minimal misfits for the two events data are 0.16 and 0.07, which are much smaller than that obtained for the data sampling the southeastern edge of the Perm Anomaly (the minimal misfit is 0.31); the large misfit has been attributed to 2-D/3-D or scattering effects (Hu and He, 2019). The small misfits here thus indicate a good agreement between the data and the preferred single-crossing models (Fig. 2b and e). We also calculated misfits with different combinations of weighting factors (Fig. S4); no difference in calculated minimal misfits has been found, indicative of stable results which have

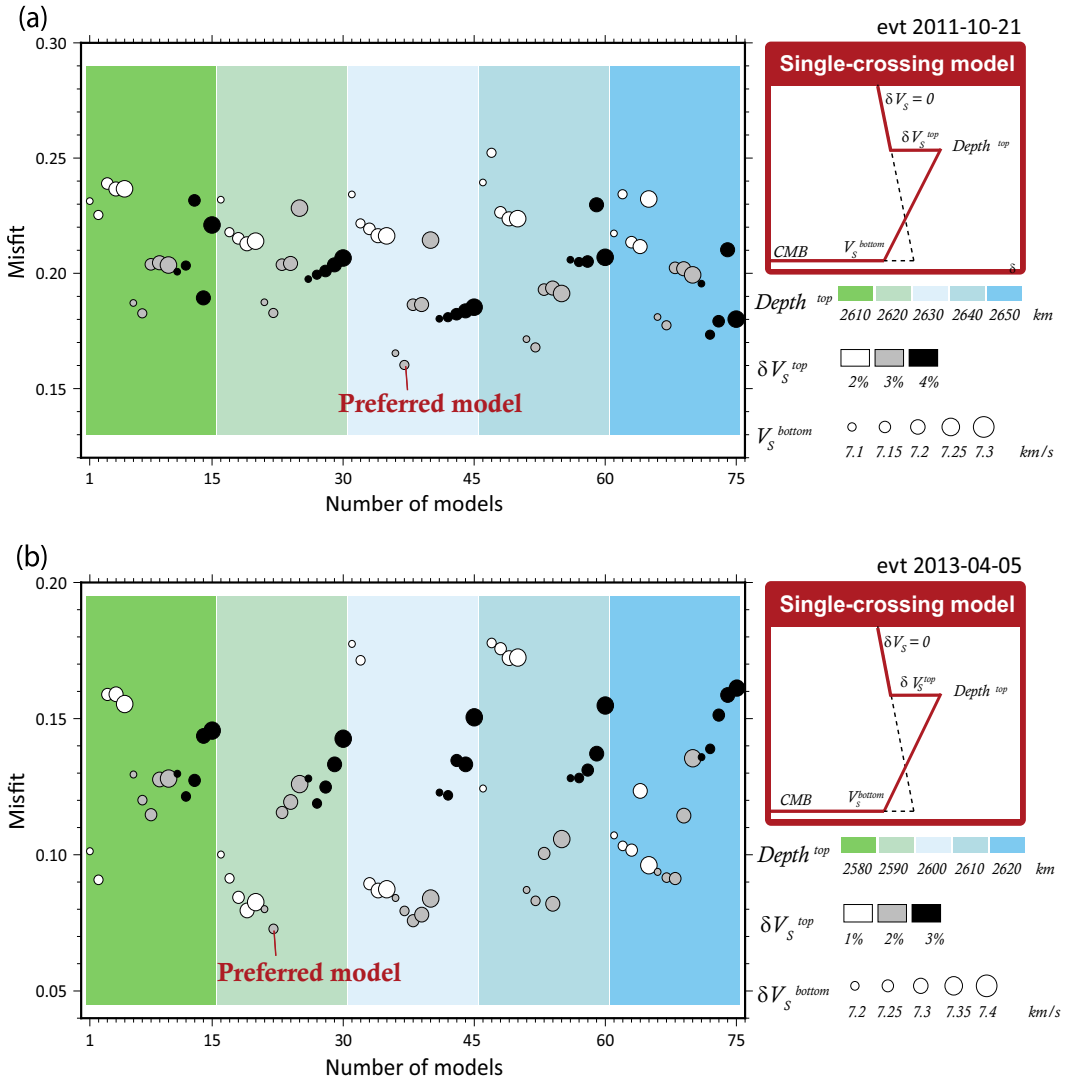


**Fig. 3.** Misfit calculated for the 75 single-crossing models for the event 2011-10-21 (a) and the event 2013-04-05 (d), respectively.

been obtained. Fig. S5 additionally demonstrates that the vespagrams calculated according to the best fit models (Fig. 2c and f) adequately reproduce the vespagrams, which were calculated for the data. Therefore, the best fit models are able to explain all the parameters — including the slownesses, arrival times, and amplitudes.

### 3.2. The double-crossing model

The minimal misfits obtained here for the double-crossing models (Fig. 4) are similar with those derived for the single-crossing models (Fig. 3), but the model misfits are seemingly insensitive to the depth variation of the D″ discontinuity; it is thus a challenge to precisely constrain the depth of the D″ discontinuity for this type of model. The velocity perturbation at the CMB is derived by finding the suitable coefficient R – a ratio between the *V s* change across the D″ discontinuity and the *V s* perturbation at the CMB – which leads to the minimal misfit (Fig. S6 in the Supporting information). Our results show that, for two regions sampled by the waves generated from both events, the depth of the D″ discontinuity and velocity change in *V s* across the D″ discontinuity are the same as those derived in the single-crossing models (Fig. 2c and f). The only difference occurs in the structure within the D″ layer (Fig. 5c and f). Specifically, the second discontinuity due to ppv-pv reverse transition for both events occurs at a depth of 90 km below the D″ discontinuity (i.e., pv-ppv transition). For the event 2013-04-05, the shear-wave velocity at the CMB is the same as that of IASP91 (Fig. 5f), while that for the event 2011-10-21 is −1.5% compared to IASP91 (Fig. 5c). We also calculated the fourth-root vespagrams according to the best fit models to compare with those derived for the data, and they exhibit good agreements (Fig. S7).

## 4. Discussion

### 4.1. Origin of the D″ discontinuity

The velocity profiles at the base of the mantle resolved in this study show that the D″ discontinuity structures exhibit moderate topographic relief (40 km) over distances of ~10° near the northeastern border of the Perm Anomaly. The laterally varied D″ structures are perhaps due to the existence of different thermal structures across the two locations. The occurrence of +2% (in the north area) and +3% (in the south area) increase in shear-wave velocity at the top of the D″ discontinuity is also consistent with the global value of +1 to +3% (Cobden and Thomas, 2013). The leading candidate for the origin of the D″ discontinuity is the phase transition from perovskite (pv) to post-perovskite (ppv) (e.g., Murakami, 2004; Oganov and Ono, 2004; Shim et al., 2004) at lowermost mantle pressure-temperature conditions, although some observations of the discontinuity appear to not reconcile with a simple phase transition (e.g., Thomas et al., 2004); a number of

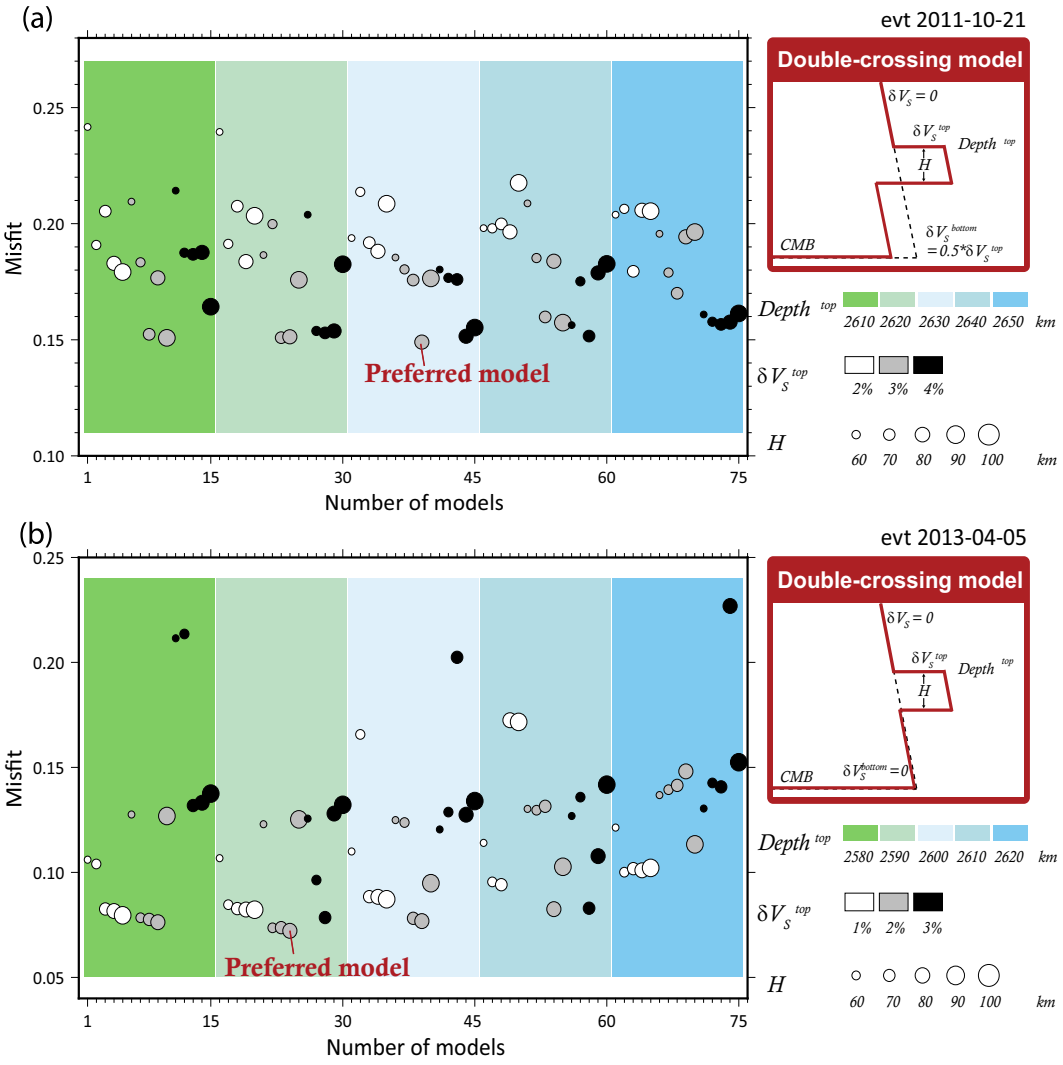


**Fig. 4.** Misfit calculated for the 75 double-crossing models for the event 2011-10-21 (a) and the event 2013-04-05 (d), respectively.

additional possibilities have been introduced, like thermal or thermo-chemical discontinuities generated by subducted slabs, alignment of anisotropic minerals and chemical heterogeneity resulting from core-mantle interactions or primitive material (Cobden and Thomas, 2013). Notably, the additional explanations are often invoked to explain D″ reflections at the base of the mantle with strong complexity, whereas our observations seem to favor a relatively simple D″ structure in the study areas.

Meanwhile, the detectability of the D″ discontinuity tightly relies on the presence of significant amounts of differentiated materials transported from the shallow mantle into the base of the mantle by subducting slabs, because mineralogical effects, in particular of Aluminum, play a critical role for the detectability of the pv-ppv boundary (i.e. the sharpness of the D″ discontinuity) (e.g., Dorfman and Duffy, 2014; Grocholski et al., 2012). Our observations are also consistent with the majority of detections that the D″ discontinuity is often located at fast regions — likely associated with accumulations of ancient slabs; for example, the discontinuity has been observed beneath the North Atlantic (Yao et al., 2015), Alaska (Sun et al., 2016), Central America (Whittaker et al., 2016), and Eurasia (Hu and He, 2019). The observations of the D″ discontinuity here thus provide evidence for the presence of a relic slab in the study areas. In addition, a velocity reduction relative to IASP91 at the CMB detected here (Fig. 2c and f) has also been observed previously (e.g., Hu and He, 2019), which has been attributed to insulation effect by long-lasting stagnation of slabs atop the CMB — leading to persistent heating from the core (e.g., Ko et al., 2017).

In this study, we only evaluate two representative types of models — including the single-crossing model and the double-crossing model. The fact is that the misfit analyses for both models yield the same parameters for the depth of the D″ discontinuity and velocity change across the D″ discontinuity, but it is hard to evaluate which type of model can better characterize the structure within the D″ layer according to the misfits alone; a more sophisticated technique like the waveform inversion approach (Kawai et al., 2007) may thus be necessary to solve the dilemma. Although the existence of a ppv-pv transition in the D″ layer has been previously suggested (Hernlund et al., 2005), Flores and Lay (2005) have argued that stacking of carefully processed seismic data is essential for reliable detection of ppv-pv boundary, because detection of a velocity decrease is much harder than detection of the shallower velocity increase due to fundamental properties of seismic waves. In addition, a later study by Kawai and Tsuchiya (2009) on seismological and mineral physics joint modeling favored a single-crossing phase transition model against a ‘ double-crossing’ model. Therefore, the issue regarding the existence of ppv-pv transition still remains unresolved, which will benefit from a future multidiscipline collaboration.

We also acknowledge that the number of models for evaluations in this study is still limited (only 75 for each model type), which has hampered our understanding of other characteristics of the D″ structure

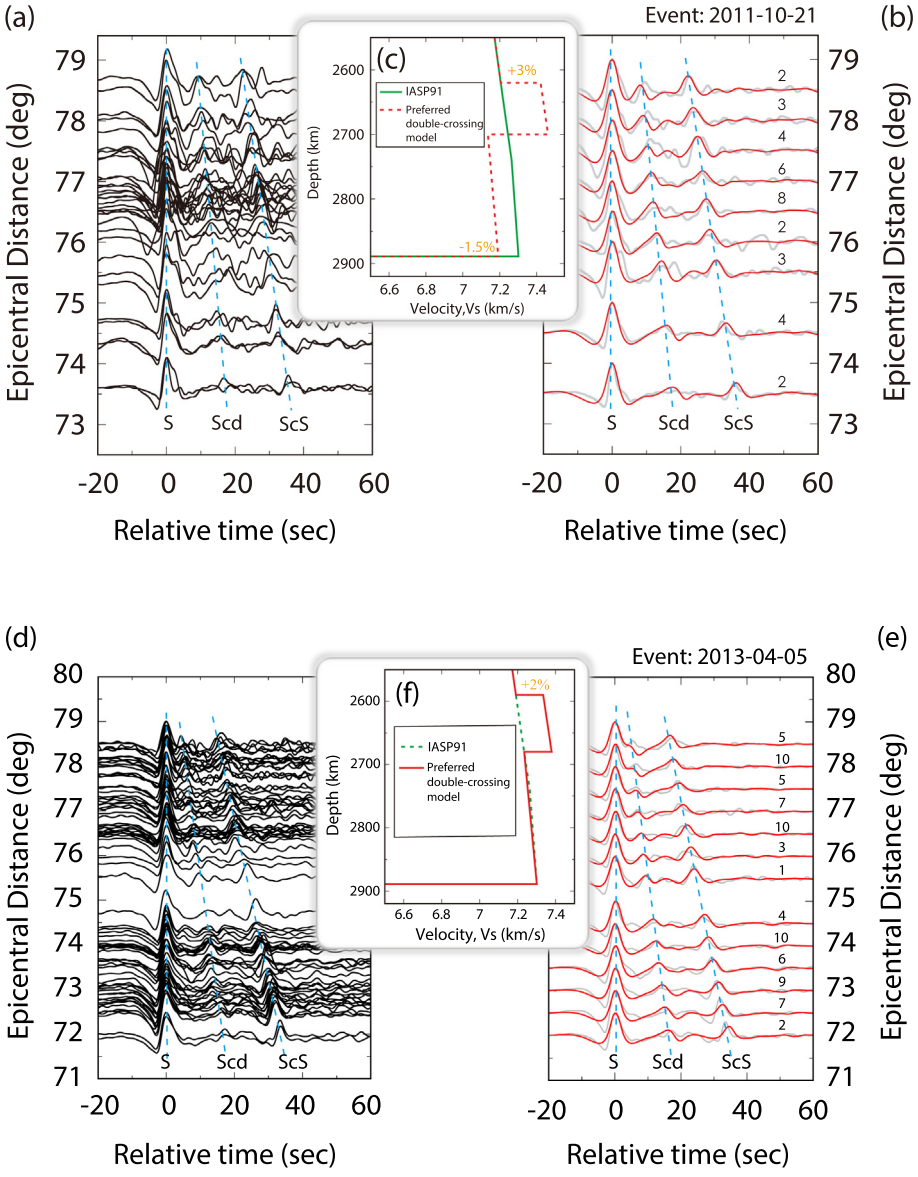


**Fig. 5.** The same as Fig. 2, but for the double-crossing models.

such as the sharpness of the D″ discontinuity (i.e., the pv-ppv transitional width); whereas the width of the ppv transition may shed light on the composition — in particular the Al-content in the D″ layer (e.g., Dorfman and Duffy, 2014; Grocholski et al., 2012). In the 75 models for each model type, we only consider a sharp D″ discontinuity (i.e., the pv-ppv transitional width = 0). If a broader transition is incorporated into the modelings, we can envisage that a larger velocity contrast across the D″ discontinuity is likely required to reconcile with the observed amplitudes of *Scd* arrivals. In other words, a given amplitude of *Scd* arrival can either be produced by a discontinuity with a broader transition but with a larger velocity increase, or produced by a discontinuity with a narrower transition but with a smaller velocity increase. Therefore, it is still a challenge to solve the trade-off between the sharpness and velocity contrast. To constrain the sharpness, modeling distance-dependence of reflected *S*-wave signals (Lay, 2008) may be one feasible approach, but most reliable observations of reflections from the D″ discontinuity are at ranges greater than 65°, and near-vertical reflections are very limited. In addition, there may have other possible limitations in this study, in particular regarding the precision and resolution of the D″ structure. Here, the increments of the depth of the D″ discontinuity and velocity jump across the D″ discontinuity were designed to be 10 km and 1%, respectively (Figs. 3 and 4), which may have limited the resolving precision of the D″ structure. In addition, the resolution also depends on the frequencies of *Scd* waves, which are usually characterized with a dominant frequency of 0.1 Hz. As a result, more detailed structures have avoided being detected. It is worth noting that, for a given depth of the D″ discontinuity, the misfits are seemingly very sensitive to the velocity variations across the D″ discontinuity (Figs. 3 and 4). As we mentioned above, the misfits exhibit less sensitive to the depth variation of the D″ discontinuity in the double-crossing models compared to the single-crossing models. Consequently, the depth of the D″ discontinuity in the double-crossing models is thus hard to be constrained precisely. Here, the errors for the varied parameters in the D″ structure are hard to be estimated due to limited number of evaluated models; according to the misfit distributions over various models (Figs. 3 and 4), we roughly evaluated that, for the single-crossing models, the uncertainty of the depth of the D″ discontinuity could be nearly or less than 10 km, and the uncertainty of the velocity jump across the D″ discontinuity could be nearly or less than 1%; whereas those for the double-crossing models are expected to be larger.

### 4.2. Lateral variations in the characteristics of the D″ discontinuity

Our observations, when combined with previous results (e.g., Cobden and Thomas, 2013; Hu and He, 2019; Lay and Helmberger, 1983; Thomas et al., 2011), show that the D″ discontinuity appears to be deepening from north to south; it is characterized with its height decreasing sequentially from 318 to 250 km (Fig. 1). A temperature variation of ~200 – 700 K is required to explain the depth variations of the D″ discontinuity, given a Clapeyron slope of ~4–14 MPa/K (Cobden et al., 2015). By contrast, the velocity jump across the D″ discontinuity remains relatively stable (2–3 %), likely indicative of less compositional variations compared to temperature in this region.

### 4.3. Origin of the paleoslab in the lowermost mantle

High velocity anomalies with a wide range of scales residing at the base of the mantle, called "slab graveyard", have been widely imaged not only by long wavelength seismic tomography (e.g., van der Meer et al., 2018) but also by high frequency precursors to *PcP* (e.g., Zhang et al., 2018) and to *PK*(*K*)*P* (e.g., Ma et al., 2016; Waszek et al., 2015). The seismic anomalies are most likely attributed to the remnants of past subducted slabs (van der Meer et al., 2010). The anomaly detected in this study is underneath Northwest Mongolia in which a number of seismic scatterers have been detected in the mid-lower mantle by analyzing out-of-plane *P*-to-*P* and *S*-to-*P* scattering energies (Schumacher and Thomas, 2016). The lower mantle anomalies have been interpreted as the remnants of the subducted Mongol-Okhotsk (MO) slab, which is also consistent with slab identification by van der Voo et al. (1999) and van der Meer et al. (2010, 2018). The MO slab has also been named the Mongol-Kazakh anomaly after its present-day location (van der Meer et al., 2018). The two locations with the D″ discontinuity detected by the two event data sets appear to align along a N–S trending (Fig. 1), which is consistent with the notion that the deepest part of the MO slab is trending N–S, whereas shallower part becomes oriented ~W–E(see the suture zone in Fig. S8 of the Supporting information), resulting from a counterclockwise rotation until Triassic time (Van der Voo et al., 2015). In addition, the slab-base depth of 2850 km inferred by van der Meer et al. (2018) favors the MO slab residing in the lowermost mantle, and their inferred slab midpoint also locates nearby the north area with the D″ discontinuity (Fig. 1). All evidence together supports the explanation that the relic slab in the lowermost mantle is most likely the subducted Mongol-Okhotsk slab. This paleoslab together with the Panthalassa and Tethyan slabs have been suggested to greatly influence the shape and location of the Perm Anomaly by numerical approach (Fritzell et al., 2016). A recent seismological study has revealed a fast anomaly in the lowermost mantle – representing the Paleotethyan lithosphere – likely residing adjacent to the southeastern edge of the Perm Anomaly (Hu and He, 2019). In addition, the location of Mongol-Okhotsk slab has been considered as the third important "anchor" slab (the first two include the Farallon and Tethyan slabs) to give longitude constraints in global subduction and absolute reference frames (van der Meer et al., 2018). Our detection will thus be beneficial to linking deep mantle structure to plate tectonic evolution.

### 4.4. Implications for seismic anisotropy in D″

Widespread seismic anisotropy has been observed at the base of the mantle (e.g., Creasy et al., 2017; He and Long, 2011; Long, 2009; Niu and Perez, 2004), in particular surrounding the LLSVPs (e.g., Cottaar and Romanowicz, 2013; Ford et al., 2015; Grund and Ritter, 2019; Lynner and Long, 2014; Wang and Wen, 2007). The mechanism for D″ anisotropy, however, still remains enigmatic. Two models have been proposed to explain it, including the shape preferred orientation (SPO) of elastically distinct materials (Kendall and Silver, 1996) and the crystallographic or lattice preferred orientation (LPO) of intrinsically anisotropic minerals (e.g., Wentzcovitch et al., 2006). Forward modeling work by Hall et al. (2004) argues against the SPO-type models because inefficient splitting occurs to *SK*(*K*)*S* phases, the LPO model may hence better explain the D″ anisotropy even though the candidate minerals like post-perovskite (ppv) and (Mg,Fe)O for deformation and slip systems remains unclear. An integrated study by Ford et al. (2015) suggested that the edge anisotropy in D″ can be best explained by invoking the LPO of ppv, with the [100] crystallographic axis oriented either nearly vertically or high obliquely to the horizontal plane. This study was based on splitting of multiple phases (*S*, *ScS*, *SKS*, and *SKKS*) encompassing a range of propagation directions along with mineral physics-based forward modeling. Nevertheless, a recent experiment reveals that ferropericlase alone can produce the observed seismic shear wave splitting in D″ in regions of downwelling, and the interplay between ferropericlase and bridgmanite CPO can explain the complex anisotropic patterns in D″ in regions of upwelling at the margin of the African LLSVP (Immoor et al., 2018).

Numerical simulations have suggested that the subducted slabs (downwellings) play an important role in controlling the deep mantle dynamics like the formation and stability of LLSVPs at the CMB (e.g., Mulyukova et al., 2015; Tackley, 2011; Tan et al., 2002, 2011), and they are thought to induce strong lower-mantle flow towards the edges of these piles where plumes rise, and their interaction with dense thermochemical piles can trigger the ascent of hot plumes that inherit chemical gradients present in D″, explaining some of the surface geochemical trends of oceanic islands (Dannberg and Gassmoller, 2018). Our seismic observations, along with previous seismic anisotropic detections (e.g., Grund and Ritter, 2019; Long and Lynner, 2015; Thomas and Kendall, 2002; Wookey and Kendall, 2008) surrounding the Perm Anomaly, may thus shed light on the dynamic processes occurring between the subducted slabs and the putative stationary LLSVPs. Specifically, the impingement of a subducted slab at the base of the mantle is thought to play a key role in shaping the anomaly (e.g., Fritzell et al., 2016), and the strong anisotropy can be developed as a result of subducted slabs interacting with the LLSVPs (e.g., Cottaar et al., 2014; Reiss et al., 2019) (Fig. 6) or the collision of subducted slabs with the core-mantle boundary (e.g., McNamara et al., 2002), although occurrence of focused upwellings (e.g., Steinberger and Torsvik, 2012) cannot be fully ruled out. At the same time, such processes reflect that the thermochemical anomalies may serve as a barrier to the flow towards their edges induced by downwellings, further indicating that the anomalies perhaps have a higher viscosity than the ambient mantle (e.g., Long and Lynner, 2015).

## 5. Summary

In this study, we find evidence for the occurrence of the D″ discontinuity associated with a relic slab (likely the subducted Mongol-Okhotsk slab) near the northeastern border of the Perm Anomaly. The impinging of the descending slab in D″ may play an important role in producing deformation via driving ambient flow towards the Perm Anomaly; this scenario is compatible with widespread seismic anisotropy observed in D″ surrounding the Perm Anomaly.

## Author contributions

J.T. with J. H. analyzed the data. C. J. contributed to the discussion of geologic interpretations. X. H. designed this study and wrote the manuscript.

## Declaration of Competing Interest

We declare that there are no conflicts of interest.

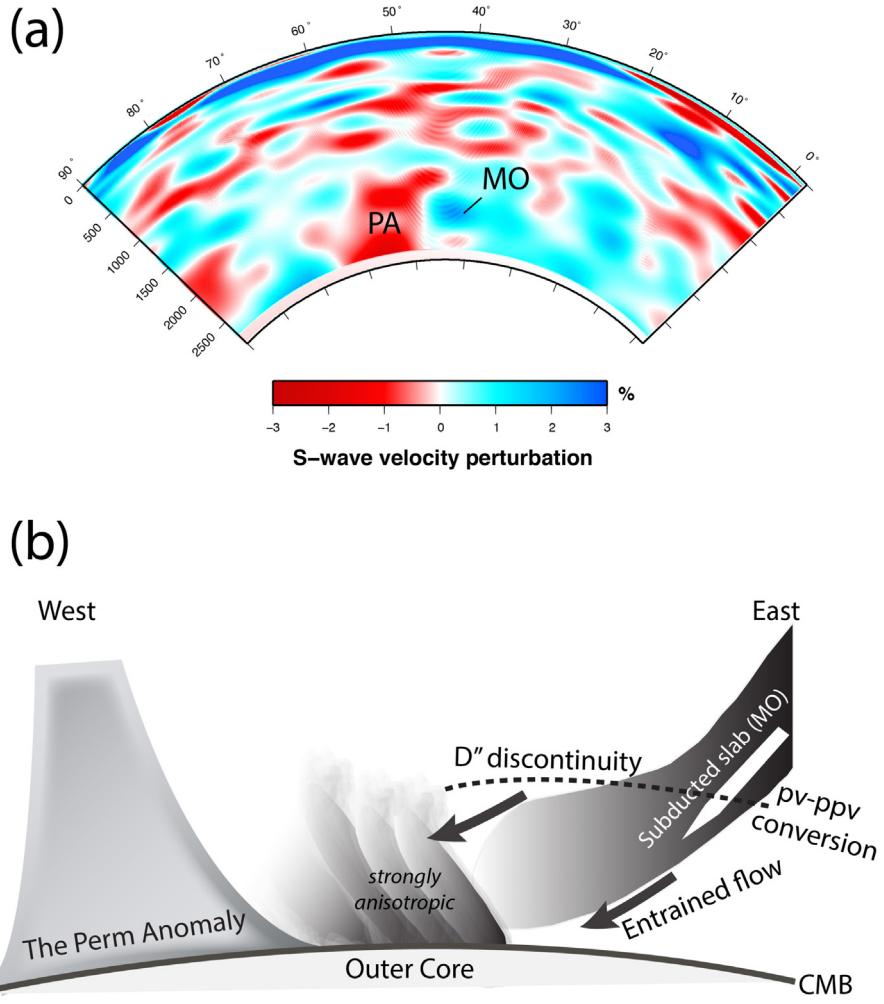


**Fig. 6.** (a) The same cross-section as that shown in Fig. 1, but with some interpretations. The quasi-vertical low velocity anomaly – rooted from the D″ layer and extended continuously to a depth of ~1500 km – is interpreted as the Perm Anomaly, whereas the fast anomaly residing to the east is likely to be the Mongol-Okhotsk slab. (b) A sketch illustrating the dynamic process of the downgoing MO slab approaching the putative stationary PA, which leads to the strong deformation as manifested with the existence of seismic anisotropy observed near the edge of the PA. MO = Mongol-Okhotsk; PA = Perm Anomaly.

## Acknowledgments

Seismic data from the European networks were accessed via the Observatories & Research Facilities for European Seismology (ORFEUS: http://www.orfeus-eu.org). The data used in this study are all freely available from ORFEUS, and can be accessed from http://doi.org/10.5281/zenodo.3514959. Some figures were prepared using Generic Mapping Tools (Wessel and Smith, 1999) and GNUPLOT. This work was funded by the National Science Foundation of China (Grants41761134051,91858205), the Laboratory for Marine Mineral Resources, Qingdao National Laboratory for Marine Science and Technology (No. MMRZZ201803), and the Public Welfare Basic Research of Zhejiang Province (No. LGF20D020001). We thank three anonymous reviewers and the Editor(Dr. Ling Chen) for their constructive and helpful comments.

## Appendix A. Supplementary data

Supplementary data to this article can be found online at https://doi.org/10.1016/j.tecto.2019.228297.

## References

Burke, K., Steinberger, B., Torsvik, T.H., Smethurst, M.A., 2008. Plume generation zones at the margins of Large Low Shear Velocity Provinces on the core-mantle boundary. Earth Planet. Sci. Lett. 265, 49–60.

Cobden, L., Thomas, C., 2013. The origin of D″ reflections: a systematic study of seismic array data sets. Geophys. J. Int. 194 (2), 1091–1118. https://doi.org/10.1093/gji/ggt152.

Cobden, L., Thomas, C., Trampert, J., 2015. Seismic Detection of Post-perovskite Inside the Earth, in The Earth's Heterogeneous Mantle. vol. 96. Springer International Publishing, Cham, pp. 391–440.

Cottaar, S., Li, M., McNamara, A.K., Romanowicz, B., Wenk, H.R., 2014. Synthetic seismic anisotropy models within a slab impinging on the core-mantle boundary. Geophys. J. Int. 199 (1), 164–177. https://doi.org/10.1093/gji/ggu244.

Cottaar, S., Romanowicz, B., 2013. Observations of changing anisotropy across the southern margin of the African LLSVP. Geophys. J. Int. 195 (2), 1184–1195.

Creasy, N., Long, M.D., Ford, H.A., 2017. Deformation in the lowermost mantle beneath Australia from observations and models of seismic anisotropy. Geophys. Res. Solid Earth 197 (1), 1. https://doi.org/10.1002/2016JB013901.

Crotwell, H.P., Owens, T.J., Ritsema, J., 1999. The TauP toolkit: flexible seismic travel-time and ray-path utilities. Seismol. Res. Lett. 70, 154–160.

Dannberg, J., Gassmoller, R., 2018. Chemical trends in ocean islands explained by plume-slab interaction. Proc. Natl. Acad. Sci. U. S. A. https://doi.org/10.1073/pnas.1714125115.

Deng, J., Long, M.D., Creasy, N., Wagner, L., Beck, S., Zandt, G., Tavera, H., Minaya, E., 2017. Lowermost mantle anisotropy near the eastern edge of the Pacific LLSVP: constraints from SKS-SKKS splitting intensity measurements. Geophys. J. Int. 210 (2), 774–786. https://doi.org/10.1093/gji/ggx190.

Dorfman, S.M., Duffy, T.S., 2014. Effect of fe-enrichment on seismic properties of perovskite and post-perovskite in the deep lower mantle. Geophys. J. Int. 197 (2), 910–919. https://doi.org/10.1093/gji/ggu045.

Dziewonski, A.M., Lekic, V., Romanowicz, B., 2010. Mantle anchor structure: an argument for bottom up tectonics. Earth Planet. Sci. Lett. 299, 69–79.

Flament, N., Williams, S., Muller, R.D., Gurnis, M., Bower, D.J., 2017. Origin and evolution of the deep thermochemical structure beneath Eurasia. Nature Commun.

https://doi.org/10.1038/ncomms14164.
Flores, C., Lay, T., 2005. The trouble with seeing double. Geophys. Res. Lett. 32 (24), 882. https://doi.org/10.1029/2005GL024366.
Ford, H.A., Long, M.D., He, X., Lynner, C., 2015. Lowermost mantle flow at the eastern edge of the African Large Low Shear Velocity Province. Earth Planet. Sci. Lett. 420, 12–22.
French, S.W., Romanowicz, B., 2015. Broad plumes rooted at the base of the Earth's mantle beneath major hotspots. Nature 525 (7567), 95–99.
Fritzell, E.H., Bull, A.L., Shephard, G.E., 2016. Closure of the Mongol-Okhotsk Ocean: insights from seismic tomography and numerical modelling. Earth Planet. Sci. Lett. 445, 1–12.
Frost, D.A., Rost, S., 2014. The P-wave boundary of the Large-Low Shear Velocity Province beneath the Pacific. Earth Planet. Sci. Lett. 403, 380–392.
Frost, D.A., Rost, S., Garnero, E.J., Li, M., 2017. Seismic evidence for Earth's crusty deep mantle. Earth Planet. Sci. Lett 470, 54–63. https://doi.org/10.1016/j.epsl.2017.04.036.
Grocholski, B., Catalli, K., Shim, S. -H., Prakapenka, V., 2012. Mineralogical effects on the detectability of the postperovskite boundary. Proc. Natl. Acad. Sci. U.S.A. 109 (7), 2275–2279. https://doi.org/10.1073/pnas.1109204109.
Grund, M., Ritter, J.R.R., 2019. Widespread seismic anisotropy in Earth's lowermost mantle beneath the Atlantic and Siberia. Geology 47 (2), 123–126. https://doi.org/10.1130/G45514.1.
Hall, S.A., Kendall, J. -M., van der Baan, M., 2004. Some comments on the effects of lower-mantle anisotropy on SKS and SKKS phases. Phys. Earth Planet. Inter. 146, 469–481. https://doi.org/10.1016/j.pepi.2004.05.002.
Haskell, N.A., 1953. The dispersion of surface waves on multilayered media. Bull. Seismol. Soc. Am. 43 (1), 17–34.
He, X., Long, M.D., 2011. Lowermost mantle anisotropy beneath the northwestern Pacific: evidence from ScS, PcS, SKS, and SKKS phases. Geochem. Geophys. Geosyst. 12, Q12012. https://doi.org/10.1029/2011GC003779.
He, X., Zheng, Y., 2018. S-to-p conversions from mid-mantle slow scatterers in slab regions: observations of deep/stagnated oceanic crust? Pure Appl. Geophys. https://doi.org/10.1007/s00024-017-1763-z.
He, Y., Wen, L., 2011. Seismic velocity structures and detailed features of the D″ discontinuity near the core-mantle boundary beneath eastern Eurasia. Phys. Earth Planet. Inter. 189, 176–184.
Hernlund, J.W., Thomas, C., Tackley, P.J., 2005. A doubling of the post-perovskite phase boundary and structure of the Earth's lowermost mantle. Nature 434 (7035), 882–886. https://doi.org/10.1038/nature03472.
Hu, J., He, X., 2019. Seismic evidence for a paleoslab in the D″ layer residing adjacent to the southeastern edge of the Perm Anomaly. Geochem. Geophys. Geosyst. https://doi.org/10.1029/2019GC008195.
Idehara, K., Tanaka, S., Takeuchi, N., 2013. High-velocity anomaly adjacent to the western edge of the Pacific low-velocity province. Geophys. J. Int. 192, 1–6.
Immoor, J., Marquardt, H., Miyagi, L., Lin, F., Speziale, S., Merkel, S., Buchen, J., Kurnosova, A., Liermanne, H. -P., 2018. Evidence for ⟨100⟩⟨011⟩ slip in ferropericlase in Earth's lower mantle from high-pressure/high-temperature experiments. Earth Planet. Sci. Lett. 489, 251–257.
Ishii, M., Tromp, J., 1999. Normal-mode and free-air gravity constraints on lateral variations in velocity and density of the Earth's mantle. Science 285, 1231–1236.
Kawai, K., Takeuchi, N., Geller, R.J., Fuji, N., 2007. Possible evidence for a double crossing phase transition in D″ beneath Central America from inversion of seismic waveforms. Geophys. Res. Lett. 34 (9), 24–55. https://doi.org/10.1029/2007GL029642.
Kawai, K., Tsuchiya, T., 2009. Temperature profile in the lowermost mantle from seismological and mineral physics joint modeling. Proc. Natl. Acad. Sci. U.S.A. 106 (52), 22119–22123. https://doi.org/10.1073/pnas.0905920106.
Kendall, J.M., Silver, P.G., 1996. Constraints from seismic anisotropy on the nature of the lower mantle. Nature 381, 409–412. https://doi.org/10.1038/381409a0.
Kennett, B.L.N., Engdahl, E.R., 1991. Traveltimes for global earthquake location and phase identification. Geophys. J. Int. 105 (2), 429–465. https://doi.org/10.1111/j.1365-246X.1991.tb06724.x.
Ko, J.Y.-T., Hung, S. -H., Kuo, B. -Y., Zhao, L., 2017. Seismic evidence for the depression of the D″ discontinuity beneath the Caribbean: implication for slab heating from the Earth's core. Earth Planet. Sci. Lett 467, 128–137. https://doi.org/10.1016/j.epsl.2017.03.032.
Lau, H.C.P., Mitrovical, J.X., Davis, J.L., Tromp, J., Yang, H.-Y., Al-Attar, D., 2017. Tidal tomography constrains Earth's deep-mantle buoyancy. Nature 551, 321–326.
Lay, T., 2008. Sharpness of the D″ discontinuity beneath the Cocos Plate: implications for the perovskite to post-perovskite phase transition. Geophys. Res. Lett. 35 (3), L143035. https://doi.org/10.1029/2007GL032465.
Lay, T., Helmberger, D.V., 1983. A lower mantle s-wave triplication and the shear velocity structure of D″. Geophys. J. Int. 75 (3), 799–837. https://doi.org/10.1111/j.1365-246x.1983.tb05010.x.
Lekic, V., Cottaar, S., Dziewonski, A., Romanowicz, B., 2012. Cluster analysis of global lower mantle tomography: a new class of structure and implications for chemical heterogeneity. Earth Planet. Sci. Lett. 357, 68–77.
Long, M.D., 2009. Complex anisotropy in D″ beneath the eastern Pacific from SKS-SKKS splitting discrepancies. Earth Planet. Sci. Lett. 285, 181–189.
Long, M.D., Lynner, C., 2015. Seismic anisotropy in the lowermost mantle near the Perm Anomaly. Geophys. Res. Lett. https://doi.org/10.1002/2015GL065506.
Lynner, C., Long, M.D., 2014. Lowermost mantle anisotropy and deformation along the boundary of the African LLSVP. Geophys. Res. Lett. 41, 3447–3454. https://doi.org/10.1002/2014GL059875.
Ma, X., Sun, X., Thomas, C., 2019. Localized ultra-low velocity zones at the eastern boundary of Pacific LLSVP. Earth Planet. Sci. Lett. 507, 40–49. https://doi.org/10.1016/j.epsl.2018.11.037.
Ma, X., Sun, X., Wiens, D.A., Wen, L., Nyblade, A., Anandakrishnan, S., Aster, R., Huerta, A., Wilson, T., 2016. Strong seismic scatterers near the core-mantle boundary north of the Pacific Anomaly. Phys. Earth Planet. Inter. 253, 21–30.
McNamara, A.K., van Keken, P.E., Karato, S.I., 2002. Development of anisotropic structure in the Earth's lower mantle by solid-state convection. Nature 310–314.
McNamara, A.K., Zhong, S., 2005. Thermochemical structures beneath Africa and the Pacific Ocean. Nature 437, 1136–1139. https://doi.org/10.1038/nature04066.
Mulyukova, E., Steinberger, B., Dabrowski, M., Sobolev, S.V., 2015. Survival of LLSVPs for billions of years in a vigorously convecting mantle: replenishment and destruction of chemical anomaly. J. Geophys. Res. Solid Earth 120 (5), 3824–3847. https://doi.org/10.1002/2014JB011688.
Murakami, M., Hirose, K., Kawamura, K., Sata, N., Ohishi, Y., 2004. Post-perovskite phase transition in $MgSiO_3$. Science 304 (5672), 855–858. https://doi.org/10.1126/science.1095932.
Ni, S., Tan, E., Gurnis, M., Helmberger, D., 2002. Sharp sides to the African superplume. Science 296, 1850–1852.
Niu, F., Perez, A.M., 2004. Seismic anisotropy in the lower mantle: a comparison of waveform splitting of SKS and SKKS. Geophys. Res. Lett. 31, L24612. https://doi.org/10.1029/2004GL0211196.
Oganov, A.R., Ono, S., 2004. Theoretical and experimental evidence for a post-perovskite phase of MgSiO3 in Earth's D″ layer. Nature 430 (6998), 445–448. https://doi.org/10.1038/nature02701.
Rao, B.P., Kumar, M.R., 2014. Seismic evidence for slab graveyards atop the Core Mantle Boundary beneath the Indian Ocean Geoid Low. Phys. Earth Planet. Inter. 236, 52–59.
Reiss, M.C., Long, M.D., Creasy, N., 2019. Lowermost mantle anisotropy beneath Africa from differential SKS-SKKS shear-wave splitting. J. Geophys. Res. https://doi.org/10.1029/2018JB017160.
Restivo, A., Helffrich, G., 2006. Core-mantle boundary structure investigated using SKS and SKKS polarization anomalies. Geophys. J. Int. 165, 288–302.
Ritsema, J., Deuss, A., Van Heijst, H., Woodhouse, J., 2011. S40RTS: a degree-40 shear-velocity model for the mantle from new Rayleigh wave dispersion, teleseismic traveltime and normal-mode splitting function measurements. Geophys. J. Int. 184 (3), 1223–1236.
Rost, S., Garnero, E.J., Stefan, W., 2010. Thin and intermittent ultralow-velocity zones. J. Geophys. Res. 115, B06312. https://doi.org/10.1029/2009JB006981.
Schumacher, L., Thomas, C., 2016. Detecting lower-mantle slab beneath Asia and the Aleutians. Geophys. J. Int. 205, 1512–1524.
Shen, X., Zhou, Y., Idehara, K., Mei, X., Xu, K., 2014. An examination of the presence and topography of the D″ discontinuity under the Russia-Kazakhstan border region using seismic waveform data from a deep earthquake in Spain. Earthq. Sci. 27 (2), 209–215. https://doi.org/10.1007/s11589-014-0071-2.
Shim, S.H., Duffy, T.S., Jeanloz, R., Shen, G., 2004. Stability and crystal structure of $MgSiO_3$ perovskite to the core-mantle boundary. Geophys. Res. Lett. 31 (10). https://doi.org/10.1029/2004GL019639.
Simmons, N.A., Forte, A., Boschi, L., Grand, S., 2010. GyPSum: a joint tomographic model of mantle density and seismic wave speeds. J. Geophys. Res. 115, B12310. https://doi.org/10.1029/2010JB007631.
Steinberger, B., Torsvik, T.H., 2012. A geodynamic model of plumes from the margins of large low shear velocity provinces. Geochem. Geophys. Geosyst. 13, Q01W09. https://doi.org/10.1029/2011GC003808.
Sun, D., Helmberger, D., Lai, V.H., Gurnis, M., Jackson, J.M., Yang, H.Y., 2019. Slab Control on the northeastern edge of the mid-Pacific LLSVP near Hawaii. Geophys. Res. Lett. 33 (6763), L07314. https://doi.org/10.1029/2018GL081130.
Sun, D., Helmberger, D., Miller, M.S., Jackson, J.M., 2016. Major disruption of D″ beneath Alaska. J. Geophys. Res. Solid Earth 121 (5), 3534–3556. https://doi.org/10.1002/2015JB012534.
Sun, N., Wei, W., Han, S., Song, J., Li, X., Duan, Y., Prakapenka, V.B., Mao, Z., 2018. Phase transition and thermal equations of state of (Fe,Al)-bridgmanite and post-perovskite: implication for the chemical heterogeneity at the lowermost mantle. Earth Planet. Sci. Lett. 490, 161–169. https://doi.org/10.1016/j.epsl.2018.03.004.
Tackley, P.J., 2011. Living dead slabs in 3-d: The dynamics of compositionally-stratified slabs entering a “slab graveyard” above the core-mantle boundary. Phys. Earth Planet. Inter. 188 (3-4), 150–162. https://doi.org/10.1016/j.pepi.2011.04.013.
Tan, E., Gurnis, M., Han, L., 2002. Slabs in the lower mantle and their modulation of plume formation. Geochem. Geophys. Geosyst. 3 (11), 124. https://doi.org/10.1029/2001GC000238.
Tan, E., Leng, W., Zhong, S., Gurnis, M., 2011. On the location of plumes and lateral movement of thermochemical structures with high bulk modulus in the 3-D compressible mantle. Geochem. Geophys. Geosyst. 12, Q07005. https://doi.org/10.1029/2011GC003665.
Thomas, C., Kendall, J.M., 2002. The lowermost mantle beneath northern Asia-II. Evidence for lower-mantle anisotropy. Geophys. J. Int. 151 (1), 296–308. https://doi.org/10.1046/j.1365-246X.2002.01760.x.
Thomas, C., Kendall, J. -M., Lowman, J., 2004. Lower-mantle seismic discontinuities and the thermal morphology of subducted slabs. Earth Planet. Sci. Lett. 225 (1-2), 105–113. https://doi.org/10.1016/j.epsl.2004.05.038.
Thomas, C., Wookey, J., Brodholt, J., Fieseler, T., 2011. Anisotropy as cause for polarity reversals of D″ reflections. Earth Planet. Sci. Lett. 307 (3-4), 369–376. https://doi.org/10.1016/j.epsl.2011.05.011.
Thomson, W.T., 1950. Transmission of elastic waves through a stratified solid medium. J. Appl. Phys. 21 (2), 89–93. https://doi.org/10.1063/1.1699629.
Thorne, M.S., Garnero, E.J., Grand, S.P., 2004. Geographic correlation between hot spots and deep mantle lateral shear-wave velocity gradients. Phys. Earth Planet. Inter. 146, 47–63.

Torsvik, T.H., Domeier, M., 2017. Correspondence: Numerical modelling of the PERM Anomaly and the Emeishan large igneous province. Nature Commun. https://doi.org/10.1038/s41467-017-00125-2.
Torsvik, T.H., Smethurst, M.A., Burke, K., Steinberger, B., 2006. Large igneous provinces generated from the margins of the large low-velocity provinces in the deep mantle. Geophys. J. Int. 167, 1447–1460.
van der Meer, D.G., Spakman, W., van Hinsbergen, D.J.J., Amaru, M.L., Torsvik, T.H., 2010. Towards absolute plate motions constrained by lower-mantle slab remnants. Nat. Geosci. 3, 36–40.
van der Meer, D.G., van Hinsbergen, D.J.J., Spakman, W., 2018. Atlas of the underworld: slab remnants in the mantle, their sinking history, and a new outlook on lower mantle viscosity. Tectonophysics 723, 309–448.
van der Voo, R., Spakman, W., Bijwaard, H., 1999. Mesozoic subducted slabs under Siberia. Nature 397, 246–249.
Van der Voo, R., van Hinsbergen, D.J.J., Domeier, M., Spakman, W., Torsvik, T.H., 2015. Latest Jurassic-earliest Cretaceous closure of the Mongol-Okhotsk Ocean: a paleomagnetic and seismological-tomographic analysis. Geol. Soc. Am. Spec. Pap. 513, 589–606.
Wang, R., 1999. A simple orthonormalization method for stable and efficient computation of Green's functions. Bull. Seismol. Soc. Am. 733–741.
Wang, Y., Wen, L., 2007. Complex seismic anisotropy at the border of a very low velocity province at the base of the Earth's mantle. J. Geophys. Res. 112, B09305. https://doi.org/10.1029/2006JB004719.
Waszek, L., Thomas, C., Deuss, A., 2015. PKP precursors: implications for global scatterers. Geophys. Res. Lett. 42, 3829–3838.
Wentzcovitch, R.M., Tsuchiya, T., Tsuchiya, J., 2006. $MgSiO_3$ postperovskite at D″ conditions. Proc. Natl. Acad. Sci. U. S. A. 103, 543–546. https://doi.org/10.1073/pnas.0506879103.
Wessel, P., Smith, W.H.F., 1999. Free software helps map and display data. Eos Trans. AGU 72, 441. https://doi.org/10.1029/90EO00319.
Whittaker, S., Thorne, M.S., Schmerr, N.C., Miyagi, L., 2016. Seismic array constraints on the D″ discontinuity beneath Central America. J. Geophys. Res. Solid Earth 121 (1), 152–169. https://doi.org/10.1002/2015JB012392.
Wookey, J., Kendall, J. -M., 2008. Constraints on lowermost mantle mineralogy and fabric beneath Siberia from seismic anisotropy. Earth Planet. Sci. Lett. 275 (1-2), 32–42. https://doi.org/10.1016/j.epsl.2008.07.049.
Wysession, M.E., Lay, T., Revenaugh, J., Williams, Q., Garnero, E.J., Jeanloz, R., Kellogg, L.H., 1998. The D″ discontinuity and its implications. In: Gurnis, M., Wysession, M.E., Knittle, E., Buffett, B.A. (Eds.), The Core-Mantle Boundary Region (Geodyn. Ser., Vol. 28). AGU, Washington,DC, pp. 273–297.
Yang, Z., He, X., 2015. Oceanic crust in the mid-mantle beneath west-central Pacific subduction zones: evidence from s to p converted waveforms. Geophys. J. Int. 203 (1), 541–547. https://doi.org/10.1093/gji/ggv314.
Yao, Y., Whittaker, S., Thorne, M.S., 2015. D″ discontinuity structure beneath the North Atlantic from Scd observations. Geophys. Res. Lett. 42 (10), 3793–3801. https://doi.org/10.1002/2015GL063989.
Zhang, B., Ni, S., Sun, D., Shen, Z., Jackson, J.M., Wu, W., 2018. Constraints on small-scale heterogeneity in the lowermost mantle from observations of near podal PcP precursors. Earth Planet. Sci. Lett. 489, 267–276.
Zhang, Y., Ritsema, J., Thorne, M.S., 2009. Modeling the ratios of SKKS and SKS amplitudes with ultra-low velocity zones at the core-mantle boundary. Geophys. Res. Lett. 36, L19303. https://doi.org/10.1029/2009GL040030.